Supporting Information

Yu-Shiba-Rusinov states in the charge-density modulated superconductor $NbSe_2$

Eva Liebhaber,[†] Sergio Acero González,[‡] Rojhat Baba,[†] Gaël Reecht,[†] Benjamin W. Heinrich,[†] Sebastian Rohlf,[¶] Kai Rossnagel,[¶,§] Felix von Oppen,[‡] and Katharina J. Franke[*,†]

[†]*Fachbereich Physik, Freie Universität Berlin, 14195 Berlin, Germany*

[‡]*Dahlem Center for Complex Quantum Systems and Fachbereich Physik, Freie Universität Berlin, 14195 Berlin, Germany*

[¶]*Ruprecht-Haensel-Labor and Institut für Experimentelle und Angewandte Physik, Christian-Albrechts-Universität zu Kiel, 24098 Kiel, Germany*

[§]*Deutsches Elektronen-Synchrotron DESY, 22607 Hamburg, Germany*

E-mail: franke@physik.fu-berlin.de

Theoretical considerations

Mean-field description of the charge-density wave

We resort to a phenomenological mean-field description. We start with a generic Fröhlich-type Hamiltonian describing electrons coupled to phonons,[1]

$$H = \sum_{\mathbf{k}} \epsilon_{\mathbf{k}} c^\dagger_{\mathbf{k}} c_{\mathbf{k}} + \sum_{\mathbf{q}} \omega_{\mathbf{q}} b^\dagger_{\mathbf{q}} b_{\mathbf{q}} + \sum_{\mathbf{k},\mathbf{q}} g_{\mathbf{q}} (b_{\mathbf{q}} + b^\dagger_{-\mathbf{q}}) c^\dagger_{\mathbf{k}+\mathbf{q}} c_{\mathbf{k}}. \tag{S1}$$

Here, $c_{\mathbf{k}}$ annihilates electrons with momentum $\mathbf{k}$ and energy $\epsilon_{\mathbf{k}}$, $b_{\mathbf{q}}$ annihilates a phonon with wavevector $\mathbf{q}$ and frequency $\omega_{\mathbf{q}}$, and $g_{\mathbf{q}}$ denotes the strength of the electron-phonon coupling. Within mean-field theory, we assume that certain phonon modes (denoted by $\mathbf{Q}$) go soft due to their coupling to the electronic system and develop a finite expectation value. Restricting to the lowest Fourier components and neglecting phonon dynamics beyond the static charge-density wave (CDW) distortions, we find the mean-field Hamiltonian

$$H = \sum_{\mathbf{k}} \epsilon_{\mathbf{k}} c^\dagger_{\mathbf{k}} c_{\mathbf{k}} + \sum_{\mathbf{k}} \sum_{\mathbf{Q}} g_{\mathbf{Q}} \langle b_{\mathbf{Q}} + b^\dagger_{-\mathbf{Q}} \rangle c^\dagger_{\mathbf{k}+\mathbf{Q}} c_{\mathbf{k}} \tag{S2}$$

for the electronic degrees of freedom. Within this approach, the CDW acts on the electrons as a periodic potential $V(\mathbf{r})$. Indeed, the electron-phonon interaction term can also be expressed in real space as

$$H_{\mathrm{el-ph}} = \int \mathrm{d}\mathbf{r} V(\mathbf{r}) \psi^\dagger(\mathbf{r}) \psi(\mathbf{r}), \tag{S3}$$

where the mean-field CDW potential takes the form

$$V(\mathbf{r}) = \sum_{\mathbf{Q}} e^{-i\mathbf{Q}\cdot\mathbf{r}} g_{\mathbf{Q}} \langle b_{\mathbf{Q}} + b^\dagger_{-\mathbf{Q}} \rangle. \tag{S4}$$

To find the vectors $\mathbf{Q}$, we consider a triangular lattice of Nb atoms with lattice vectors

$$\mathbf{a}_1 = a(1, 0), \tag{S5}$$

$$\mathbf{a}_2 = a(1/2, \sqrt{3}/2) \tag{S6}$$

and bond length $a = 3.445\,\text{Å}$. The corresponding reciprocal lattice vectors $\mathbf{b}_i$ satisfying $\mathbf{a}_i \cdot \mathbf{b}_j = 2\pi\delta_{ij}$ are

$$\mathbf{b}_1 = \frac{4\pi}{\sqrt{3}a}(\sqrt{3}/2, -1/2), \tag{S7}$$

$$\mathbf{b}_2 = \frac{4\pi}{\sqrt{3}a}(0, 1). \tag{S8}$$

The unit cell of the CDW has a linear dimension which is approximately three times larger than the unit cell of the atomic lattice, $\mathbf{a}^{\text{cdw}} \approx 3\mathbf{a}_i$ (for $i = 1, 2$). Correspondingly, the reciprocal lattice vectors of the CDW are approximately a factor of three smaller, $\mathbf{b}_i^{\text{cdw}} \approx \mathbf{b}_i/3$. Then, the first harmonics of the CDW have wavevectors

$$\begin{aligned}
\mathbf{Q}_1 &= q(1-\delta)(\sqrt{3}/2, -1/2), \\
\mathbf{Q}_2 &= q(1-\delta)(0, 1), \\
\mathbf{Q}_3 &= q(1-\delta)(-\sqrt{3}/2, -1/2) = -(\mathbf{Q}_1 + \mathbf{Q}_2),
\end{aligned} \tag{S9}$$

where $q = \frac{4\pi}{3\sqrt{3}a}$, and $\delta \ll 1$ accounts for the fact that the CDW is not exactly commensurate with the lattice.

Tight-binding model

To illustrate the effect of the CDW on the YSR state wavefunction, we perform model calculations within an effective tight-binding description. Specifically, we implement a model for the $NbSe_2$ band structure first introduced in Ref.[2] and later used in Refs.[3–7]. The model

uses that the relevant states near the Fermi energy have mostly Nb character and therefore focuses on one atomic d-orbital per niobium atom. (The model neglects an additional band centered at the Γ point which predominantly derives from Se orbitals and has strongly three-dimensional character.[8]) Reducing the band-structure problem to the triangular Nb lattice makes it necessary to include hopping up to fifth nearest neighbors to reproduce the $NbSe_2$ band structure. The resulting band structure

$$E(\mathbf{k}) = t_0 + t_1(2\cos\xi\cos\eta + \cos 2\xi) + t_2(2\cos 3\xi\cos\eta + \cos 2\eta) + t_3(2\cos 2\xi\cos 2\eta + \cos 4\xi) + t_4(\cos\xi\cos 3\eta + \cos 5\xi\cos\eta + \cos 4\xi\cos 2\eta) + t_5(2\cos 3\xi\cos 3\eta + \cos 6\xi) \tag{S10}$$

is sixfold symmetric about the Γ point. Here, we defined $\xi = k_x/2$ and $\eta = \sqrt{3}k_y/2$. The

Table S1: Values of the fitting parameters t_n in Eq. (S10) in meV.

	t_0	t_1	t_2	t_3	t_4	t_5
band 1	10.9	86.8	139.9	29.6	3.5	3.3
band 2	203.0	46.0	257.5	4.4	-15.0	6.0

hopping strengths t_n are used as fitting parameters to reproduce the $NbSe_2$ band structure. The values of the parameters t_n are given in Table S1[6] for the two bands. The parameters for band 1 reproduce the inner cylindrical bands of $NbSe_2$, while the parameters for band 2 reproduce the outer bands. Figure S1a shows the Fermi surfaces of the two bands, with the Brillouin zone outlined in gray.

While this model accounts for the symmetries of the band structure and the approximate shapes of the Fermi surfaces, it is limited in other ways. The model neglects interlayer coupling which, however, is expected to be weak compared to the intralayer couplings. In this approximation, it suffices to consider a single (tri)layer of $2H$-$NbSe_2$, consisting of a Nb layer sandwiched between two Se layers with equal orientations of the triangles. The model also neglects spin-orbit coupling.[9] This precludes a one-to-one identification of the two sets

of bands in Fig. S1a with specific spin directions.

The elementary layer of bulk $2H$-$NbSe_2$ consists of two trilayers with the orientations of the Se lattices rotated by 180° with respect to one another. Neglecting interlayer coupling, the band structure of the second trilayer is identical to the first (but differs in the spin assignments). Thus, the bulk crystal has twofold degenerate bands, consistent with the fact that it has an inversion center located between the trilayers. The adatom predominantly couples to one of the trilayers and the band structure in Eq. (S10) should be a good starting point. In the following, we follow Ref.[7] in neglecting the splitting between the two sets of bands and model the system either by band 1 or band 2, taking these bands as spin degenerate.

Superconductivity is included by incorporating the tight-binding Hamiltonian into a Bogoliubov-deGennes Hamiltonian with conventional (isotropic) s-wave pairing. We choose the pairing strength to be $\Delta = 1\,\mathrm{meV}$. In experiment, one finds multiple coherence peaks for $2H$-$NbSe_2$. Since we focus on YSR states far from the gap edge, we choose a representative value for Δ which falls into the range of the peak distribution ($0.7 - 1.4\,\mathrm{meV}$) found in experiment.

The multiple coherence peaks originate from multiband or anisotropic superconductivity, or both. Our modeling does not account for these effects. In principle, an anisotropic gap function affects the wavefunction patterns of the YSR states. However, the (observable) spatial extent of YSR states is smaller than the coherence length through which effects of the pairing function would enter. We thus expect that the effect of an anisotropic pairing function on the YSR wavefunctions is weak and therefore account for superconductivity via an isotropic pairing function.

Coupling to the magnetic impurity

While the origin of the magnetic moment and the resulting exchange coupling can be understood starting with an Anderson model and its mapping to a Kondo Hamiltonian in the

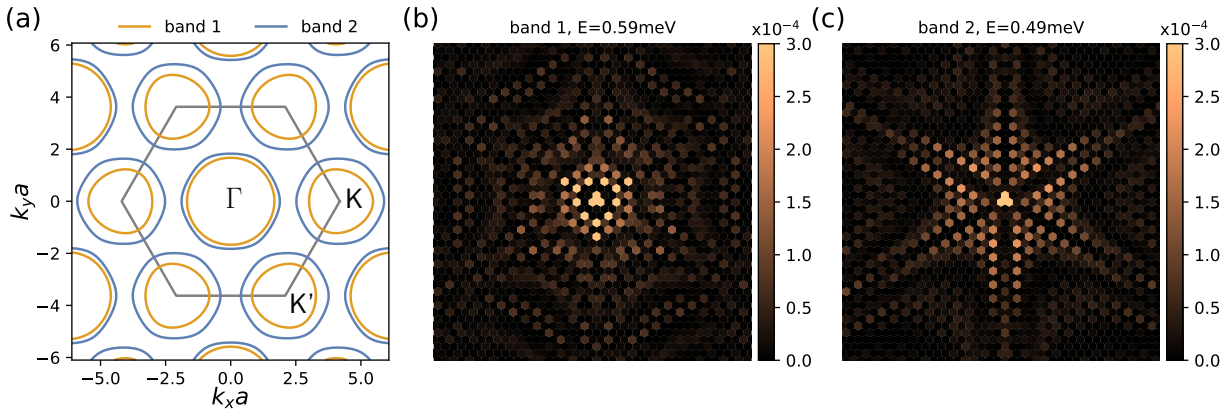

Figure S1: (a) Fermi surfaces of bands 1 and 2 (see Eq. (S10) and Table S1). (b,c) Electronic probability density $|u(\mathbf{r})|^2$ of the YSR state in the absence of the CDW for $JS/2 = 120\,\mathrm{meV}$, $K = 0$ and a lattice of size 504×504 with periodic boundary conditions for band 1 (b) and band 2 (c). The region shown includes 40×40 lattice spacings.

absence of valence fluctuations (see Ref.[10] for an extensive pedagogical discussion), YSR states are typically well described within a model which treats the impurity spin in the Kondo model as classical.[11–13] For YSR states in $NbSe_2$, this model was previously used in Ref.[7]. Following this reference, we model a magnetic impurity as a classical spin S which interacts with the substrate electrons through the exchange interaction $JS\sigma_z/2$ and accompanying potential scattering K. In our experiment, we focus on magnetic impurities located above the center of a Nb triangle (hollow-centered, see Fig. 1b of the main text). The impurity induces not only separate exchange and potential couplings to its three neighbors, but also nonlocal exchange couplings which scatter electrons between the three sites via the impurity. It is essential to retain the latter to ensure that the impurity induces only one pair of YSR resonances. If we assume identical hopping amplitudes between the three sites and the impurity and assume that the impurity spin is aligned along the z-direction, we obtain the exchange coupling

$$H_{\mathrm{exch}} = -\frac{JS/2}{3} \sum_{i,j} \sum_{s,s'} c_{is}^{\dagger} \sigma_{ss'}^{z} c_{js'} \tag{S11}$$

and potential scattering terms

$$H_{\mathrm{pot}} = \frac{K}{3} \sum_{i,j} \sum_{s} c_{is}^{\dagger} c_{js}. \tag{S12}$$

Here, the sums over i and j run over the three nearest-neighbor Nb sites of the impurity, σ^z denotes a Pauli matrix, and c_{is} annihilates an electron on site i with spin s.

Figures S1b and c show the probability densities of the YSR states for (a spin-degenerate version of) bands 1 and 2, respectively, for a specific choice of impurity parameters. The spatial distribution of the probability density is threefold symmetric in both cases. Due to the more isotropic character of band 1, the corresponding YSR state is also more spatially isotropic than its band 2 counterpart, which exhibits a more pronounced anisotropy. In a more realistic modeling including the effects of spin-orbit coupling on the band structure (but within the approximation that the impurity is coupled only to a single trilayer), the YSR states would be simultaneously coupled to spin-textured, but polarized versions of both bands. While this implies that our results for the YSR wavefunctions are only qualitative, the symmetry of the YSR wavefunctions should not be affected by this approximation. Similarly, we expect that the qualitative variation of the YSR energies with the location of the adsorption site relative to the CDW would also be unaffected.

We note that in our approximation, there is only a single pair of YSR states for a classical magnetic impurity. In fact, this conclusion would remain valid even when spin-orbit splitting of the bands was taken into account. On the one hand, it is known that even in multiband situations, a classical magnetic impurity induces only a single pair of YSR states. In fact, if we write the matrix of exchange couplings $J_{\alpha\alpha'}$ between bands α and α', it rather robustly satisfies the relation $J_{11}J_{22} = J_{12}J_{21}$. With this relation, a classical magnetic impurity generates only a single pair of YSR states. For instance, this was shown explicitly for a generic model motivated by the multiband superconductor MgB_2[14] and for a quantum dot coupled to multiple superconducting leads.[15] In the presence of spin-orbit coupling, the same

conclusions can be shown to remain valid. This can be seen by expressing the Hamiltonian in terms of creation and annihilation operators for Kramers pairs of electron states rather than conventional spin states.

Coupling to the charge-density wave

As explained above, the effect of the CDW on the electrons of the substrate can be described through a periodic potential. Within the tight-binding model, we include the CDW as a modulation of the on-site potential,

$$H_{\mathrm{cdw}} = \sum_{\mathbf{r},\sigma} c^{\dagger}_{\mathbf{r}\sigma} V(\mathbf{r}) c_{\mathbf{r}\sigma}, \tag{S13}$$

where the sum runs over the lattice sites of the triangular Nb lattice. The CDW potential $V(\mathbf{r})$ is constructed from the main Fourier components of the CDW [see Eq. (S9)],

$$V(\mathbf{r}) = V_0 \left[\cos(\mathbf{Q}_1 \cdot \mathbf{r} + \phi_1) + \cos(\mathbf{Q}_2 \cdot \mathbf{r} + \phi_2) + \cos(\mathbf{Q}_3 \cdot \mathbf{r} + \phi_3)\right], \tag{S14}$$

where V_0 denotes the amplitude of the CDW potential. Except for $\phi_1 = \phi_2 = \phi_3$ and similar fine-tuned cases, typical choices of the phases ϕ_i yield CDW potentials with the desired symmetry and shape, exhibiting an absolute maximum, an absolute minimum, and a local minimum/saddle point. For definiteness, we choose $\phi_1 = \phi_2 = 0$.

Due to the small deviations from commensurability, the CDW shifts slowly as a function of position relative to the underlying atomic lattice. On the scale of the YSR states, these shifts can be considered constant so that the CDW potential can be written as

$$V(\mathbf{r}) = V_0 \left[2\cos\left(\sqrt{3}\frac{q}{2}(x - x_0)\right)\cos\left(\frac{q}{2}(y - y_0)\right) + \cos\left(q(y - y_0) + \phi_3\right)\right], \tag{S15}$$

where $q = 4\pi/3\sqrt{3}$. The offsets x_0 and y_0 originate from the deviation δ from commensurability, and describe the local shift of the CDW relative to the atomic lattice. In the

experiment, the measured maxima of the CDW correspond to regions where the lattice deformation compresses the ions, creating an attractive potential for the electrons. For this reason we choose the potential $V(\mathbf{r})$ to have minima where the measured tunneling density of states has maxima, *i.e.*, position I of the adatom corresponds to a minimum of $V(\mathbf{r})$ and position III corresponds to a maximum. In principle, the CDW may also modulate the hopping parameters of the tight-binding model, but the effective long-range hopping processes of the model make this cumbersome to include.

We note that this model also includes configurations of the CDW relative to the atomic lattice which are not observed experimentally (see Fig. S18). Theoretical results for these unobserved configurations are only included for completeness. The results for observed configurations are not affected since the Moire-like variations occur on relatively large scales.

Numerical results

Within this model, we can study how the wavefunction and the energy of YSR states depend on the adatom position relative to the CDW. As discussed above, the model cannot reproduce the experimental results quantitatively as it neglects various relevant effects. Nevertheless, the model is expected to capture the symmetries of the YSR wavefunctions and to provide insights into the qualitative dependence of the YSR energy on the adsorption site relative to the CDW. Figure S2 shows the probability density of the YSR wavefunction for the six different positions of the adatom relative to the CDW, as discussed in the main text. The results are obtained for the parameters of band 2. The adatoms in positions I and III are at the maximum and the minimum of the CDW, respectively, *i.e.*, at points with a threefold symmetric environment. Consequently, the corresponding density plots (Fig. S2a and c) present threefold symmetry. Positions II, IV, and V exhibit reflection symmetry about an axis that passes through the adatom. For the corresponding plots shown in Fig. S2b, d, and e, this axis is aligned along the vertical direction. Finally, position VI has no symmetries with respect to the CDW and consequently, the state shown in Fig. S2f also exhibits no

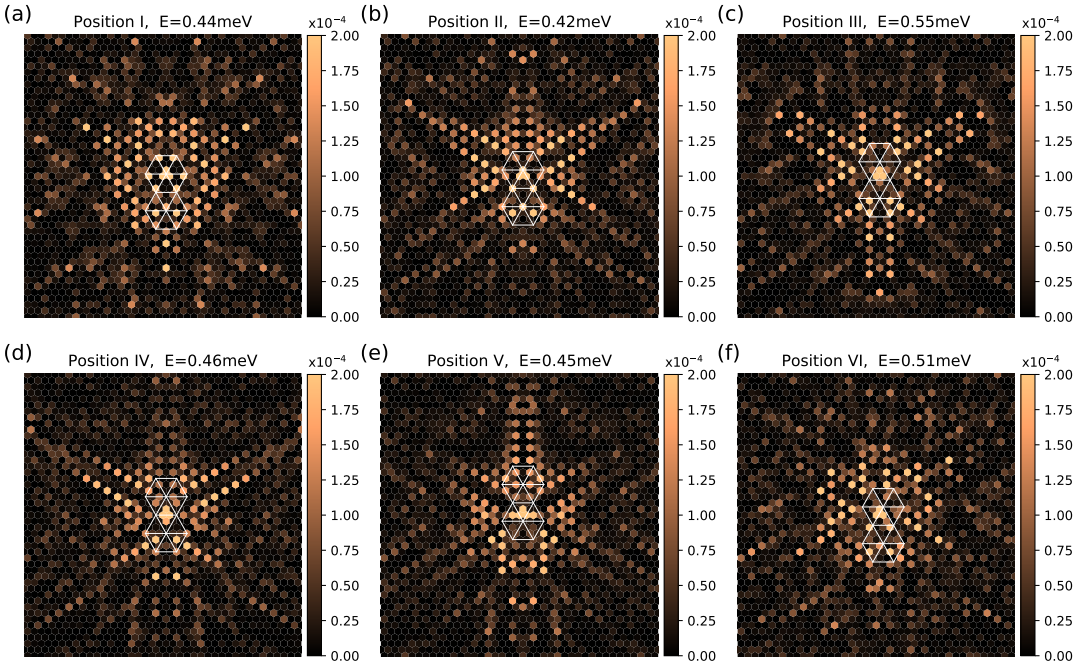

Figure S2: Electronic probability density $|u(\mathbf{r})|^2$ of the YSR state in the presence of the CDW potential for band 2 and for adatoms located at positions equivalent to those studied experimentally as presented in the main text. For all plots, the parameters are $JS/2 = 120\,\text{meV}$, $K = 0$, $V_0 = -30\,\text{meV}$, $\phi = \pi/3$ and a lattice of size 504×504 with periodic boundary conditions. The region shown includes 40×40 lattice spacings. The white lines outline the CDW, with crossing lines indicating a maximum of the CDW.

symmetries. Interestingly, the YSR state seems to retain the original threefold symmetry (without CDW) to some degree (compare with Fig. S1c).

Figure S3 shows equivalent plots for band 1. Due to the more isotropic character of band 1, the threefold symmetry is less pronounced in these plots. Remarkably, position VI (Fig. S3f) does not preserve any of the original threefold symmetry in the vicinity of the adatom. More generally, a comparison between Figs. S2 and S3 shows that the detailed YSR wavefunctions depend quite sensitively on the band structure parameters.

Finally, we discuss the correlation of the energy of the YSR state with the modulation of the local density of states by the CDW, as shown in Fig. 4 in the main text. Within a simple model of a classical magnetic impurity, the energy of YSR states depends on the strength

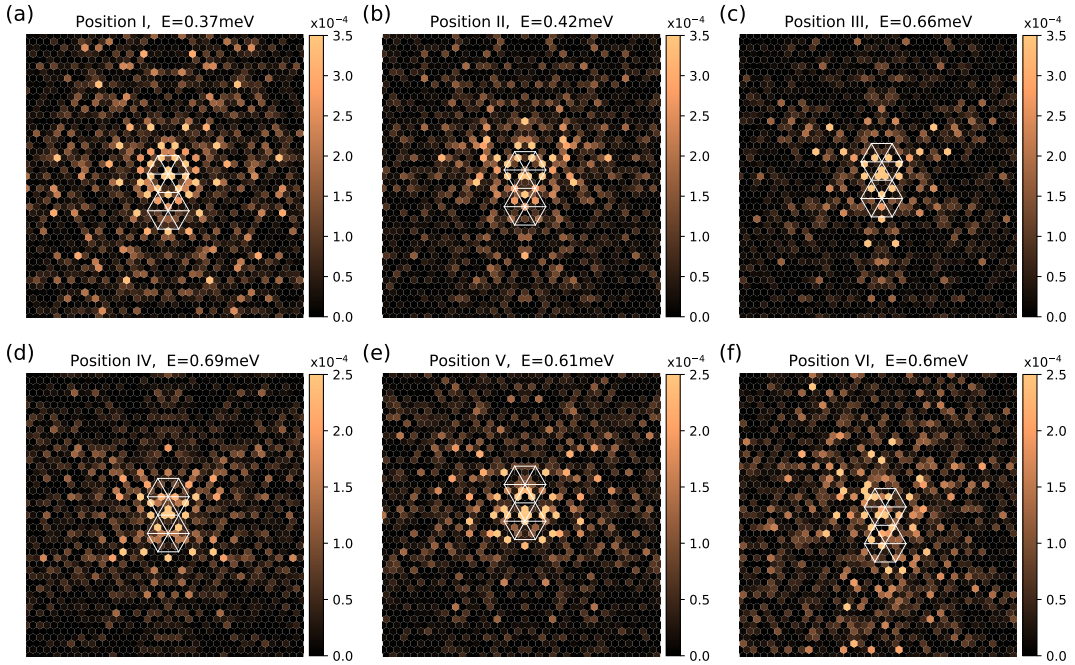

Figure S3: Analogous plots to those in Fig. S2 for band 1. Parameters: $JS/2 = 120\,\mathrm{meV}$, $K = 0$, $V_0 = -30\,\mathrm{meV}$, $\phi = \pi/3$ and a lattice of size 504×504 with periodic boundary conditions. The region shown includes 40×40 lattice spacings.

of the exchange coupling as measured by the dimensionless parameter $\alpha = \pi\nu_0 JS/2$, where ν_0 is the density of states, J the exchange coupling, and S the impurity spin. Thus, one indeed expects the energy of the YSR state to depend on the density of states ν_0. The direction of the energy shift depends on whether the impurity is weakly or strongly coupled, corresponding to unscreened or (partially) screened impurity spins, respectively. The energy of the positive-energy YSR state decreases (increases) with the density of states, depending on whether the impurity spin is unscreened (screened). Variations in the local density of states due to the CDW should thus be reflected in the energy of the YSR states. Within this picture, the observed correlations suggest that in our experiment the impurity is in the strong-coupling limit.

This interpretation is consistent with our theoretical results. However, we find that in general the CDW affects the energy of the YSR state through two mechanisms. In addition

to the density of states effect, the CDW potential has a second effect which can be roughly rationalized as the CDW affecting the strength of potential scattering from the impurity and thereby shifting the YSR energy. Including potential scattering within the simple model, the energy of a YSR state is given by[11,13,16]

$$E = \pm\Delta \frac{1-\alpha^2+\beta^2}{\sqrt{4\alpha^2+(1-\alpha^2+\beta^2)^2}}, \tag{S16}$$

where $\beta = \pi\nu_0 K$ is a dimensionless measure of the strength of the potential scattering K. The transition between weak and strong coupling takes place at $\alpha^2 = 1+\beta^2$ where the energy of the YSR state passes through zero. Roughly, the CDW potential V seems to shift K to $K + V(\mathbf{r}_0)$, where $\mathbf{r}_0$ denotes the adsorption site of the impurity. For comparison with experiment, it is important to note that an increase in the CDW potential *decreases* the density of states. This can be seen in *e.g.* Fig. S4g, which shows numerical results for the average local density of states of the three sites coupled to the impurity (orange) in the presence of the CDW potential (blue) as obtained from a straight-forward band structure calculation. Thus, the experiment implies an anticorrelation between the CDW potential V and the energy of the YSR states.

To illustrate these two effects of the CDW potential, we calculate the YRS energy for different adatom positions and various values of K. Consider first the results for weak coupling. We find that depending on the strength K of potential scattering, the CDW potential is correlated or anticorrelated with the energy of the YSR state. For $K = 180\,\text{meV}$ and $K = 0$, the energy is correlated with the CDW potential, see Fig. S4c and d. In contrast, we find anticorrelations for $K = -180\,\text{meV}$, see Fig. S4b. The correlations observed at $K = 0$ are consistent with the effect of the CDW potential on the density of states. At this K, the energy shift of the YSR state due to the change in potential scattering, K to $K + V(\mathbf{r}_0)$, is weak since the energy of the YSR states is only weakly dependent on K near the minimum at $K = 0$. This is illustrated in Fig. S4a which shows the dependence of the energy of the

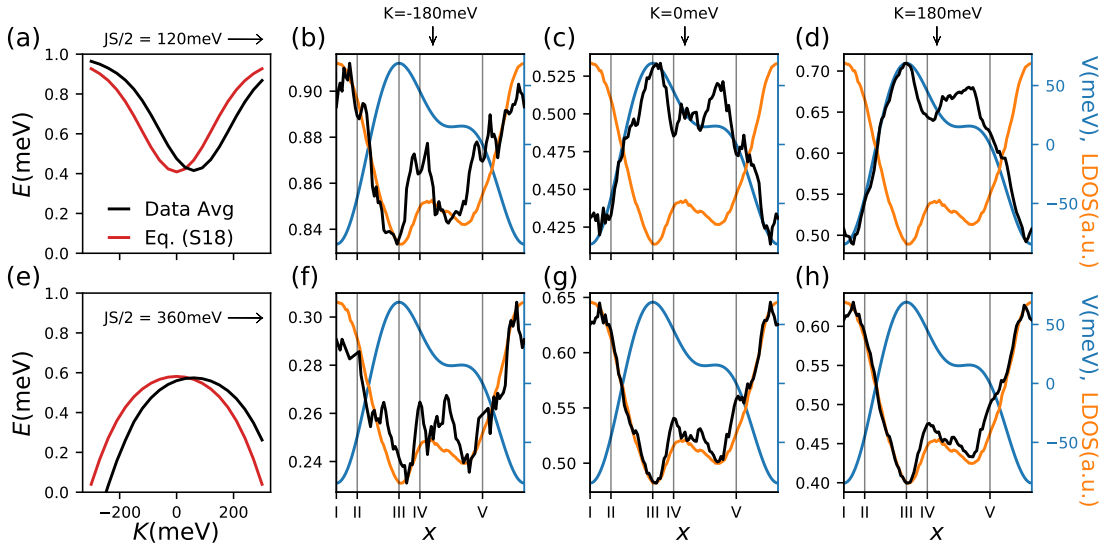

Figure S4: Tight-binding calculations for the energy of the YSR state as a function of the position of the adatom relative to the CDW, for various potential scattering strengths K. Panels (a) and (e) show the energy of the YSR state E vs. K for the weakly and strongly coupled regimes, respectively [as obtained by averaging over different positions of the adatom relative to the CDW (black) and as given by Eq. (S16) for an appropriately chosen ν_0 (red)]. Panels (b)-(d) show E vs. adatom position in the weakly coupled regime for three different K. The plots show the local density of states (LDOS, orange) to anticorrelate with the CDW potential V (blue). Panels (c) and (d) show the energy to correlate with the CDW potential V (anticorrelate with the LDOS). For $K = -180\,\mathrm{meV}$ shown in panel (b) the correlation inverts due to the shift of K to $K + V(\mathbf{r}_0)$ (see text). Panels (f)-(h) show equivalent plots for the strongly coupled regime, where the effect of K is less relevant. The energy E is correlated with the LDOS as expected from Eq. (S16). For all plots, the parameters are $V_0 = -30\,\mathrm{meV}$, $\phi = \pi/3$, and a lattice size of 750×750.

YSR state on K in the weak-coupling regime. Specifically, the black curve averages data for the energy of the YSR state over different adatom positions. The red curve corresponds to Eq. (S16) with the same values for JS and K and an appropriately chosen density of states ν_0. Both curves exhibit similar 'parabolic' behaviors.

For the strongly coupled regime, we find anticorrelations between the CDW potential and the energy of the YSR state – and thus correlations between the local density of states and the YSR energy – for all values of K, see Fig. S4f,g and h. These correlations between the density of states and the YSR energy are consistent with experiment. To start with, the anticorrelations at $K = 0$ are consistent with the expected density of states effect according

to Eq. (S16). For strong coupling, the dependence of the YSR energy on K is generally weaker compared to the weak coupling case, see Fig. S4e. For this reason, the shift of K by the CDW potential no longer overcomes the density-of-states effect. Thus, unless the impurity is a surprisingly strong potential scatterer, we conclude that in experiment the impurity is in the strong coupling limit.

Experimental details

Superconducting tip

In order to increase the energy resolution beyond the Fermi-Dirac limit, all measurements presented in the manuscript were performed using a superconducting Pb tip fabricated by indenting a W tip into a clean Pb(111) surface until the tip exhibits a bulk-like superconducting gap. Details of the preparation procedure for tip and sample are described in Ref.[17]. The tunneling current is proportional to the convolution of the density of states of the sample ρ_S and tip ρ_t and can be expressed as:[18]

$$I(V) \propto \int_{-\infty}^{+\infty} \mathrm{d}E \; \rho_\mathrm{t}(E-eV,T)\rho_\mathrm{s}(E,T)[f(E-eV,T)-f(E,T)]|M_{\mu,\nu}|^2 \; . \tag{S17}$$

Here, $f(E,T)$ is the Fermi-Dirac-distribution function accounting for the thermal occupation of the states in the tip and the sample, and $|M_{\mu,\nu}|$ is the tunneling matrix element between the initial state μ and final state ν.

This leads to the differential conductance:

$$\begin{aligned}\frac{\partial I}{\partial V} \propto \int_{-\infty}^{+\infty} \mathrm{d}E \; & \frac{\partial \rho_\mathrm{t}(E-eV)}{\partial V}\rho_\mathrm{s}(E,T)[f(E-eV,T)-f(E,T)] \\ & + \int_{-\infty}^{+\infty} \mathrm{d}E \; \rho_\mathrm{t}(E-eV)\rho_\mathrm{s}(E,T)\frac{\partial f(E-eV,T)}{\partial V} \; .\end{aligned} \tag{S18}$$

Before investigating the $NbSe_2$ sample, the tip was characterized on a clean Pb(111) sample.

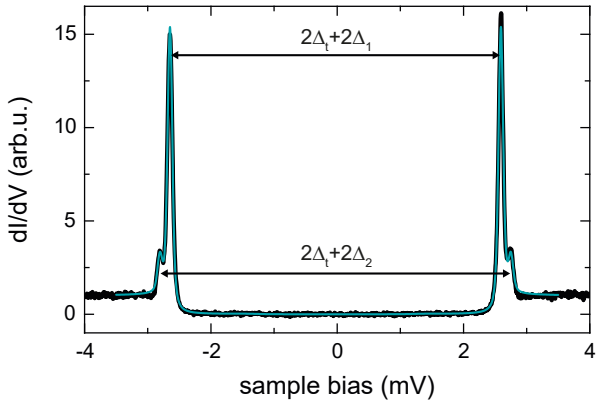

Figure S5: Constant-height spectrum taken with a Pb tip on a bare Pb(111) crystal (set point: 4 mV, 200 pA; $T = 1.1\,\mathrm{K}$). The fit (shown in green) is performed as described in Ref.[19].

A spectrum taken on bare Pb(111) after preparation of the Pb tip is shown in Fig. S5. The two superconducting energy gaps of the substrate are well resolved.[19] The Pb tip was characterized by the fit procedure described in detail in Ref.[19] where a BCS-like density of states is assumed for the tip:

$$\rho_\mathrm{t}(E) = \mathrm{sgn}(E)\,\Re\left(\frac{E - i\Gamma}{\sqrt{(E - i\Gamma)^2 - \Delta_\mathrm{t}^2}}\right). \tag{S19}$$

From this fitting procedure we determine the values for the superconducting energy gap Δ_t and the depairing factor Γ of the tip. The size of the energy gap $\Delta_\mathrm{t} \approx 1.35$ meV does not vary for bulk-like tips, whereas the depairing factor was found to vary between $\Gamma \approx$ 10-20 μeV for different tips.

Numerical deconvolution of the $\mathrm{d}I/\mathrm{d}V$ spectra

In order find the exact position of the YSR energies on the $NbSe_2$ sample, all data was numerically deconvolved as described in the following (similar to the procedure described in Ref.[20]). Equation (S18) can be discretized into matrix form and then reads:

$$\frac{\overrightarrow{\partial I}}{\partial V}(V) \propto \mathbf{K}(E, V, T)\,\overrightarrow{\rho_\mathrm{s}}(E)\,. \tag{S20}$$

The vector on the left hand side contains the differential conductance data, $\overrightarrow{\rho_s}(E)$ is the local density of states of the sample. The matrix $\mathbf{K}$ can be determined by comparing Eq. (S18) and Eq. (S20) to

$$\mathbf{K}_{ij}(E_j, V_i, T) = \mathrm{d}E\ \frac{\partial \rho_t(E_j - eV_i)}{\partial V}[f(E_j - eV_i, T) - f(E_j, T)] + \mathrm{d}E\ \rho_t(E_j - eV_i)\frac{\partial f(E_j - eV_i, T)}{\partial V}\ . \tag{S21}$$

Thus, with the knowledge of the depairing factor and the energy gap of the tip, $\rho_s(E)$ can be calculated by finding the pseudoinverse of $\mathbf{K}$. In order to assure that the tip properties did not change during sample exchange from Pb to $NbSe_2$, we checked the accurateness of the tip's energy gap by deconvolution and recalculation of spectra on several Fe adatoms. If an inaccurate value of the energy gap is assumed for the tip, the energies of the thermally excited YSR resonances are found in a wrong position in the recalculated trace. Before deconvolving all spectra are normalized and smoothed using a Savitzky-Golay filter. Deconvolved spectra of atoms I-VI (*cf.* Fig. 2 in the main text) are shown in Fig. S6.

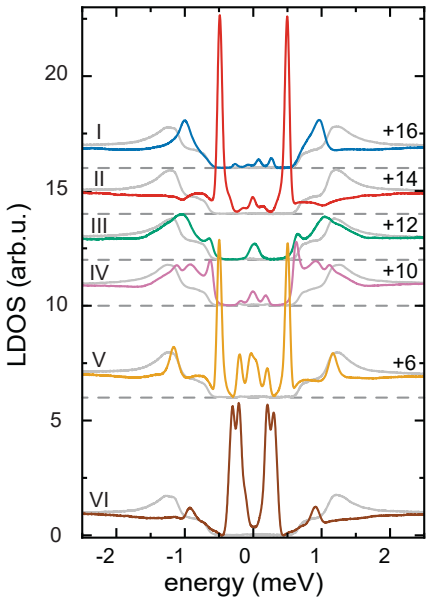

Figure S6: Deconvolved data of atom I-VI (substrate data is shown in grey). Offsets are indicated by the numbers on the right of each trace.

Identification of adsorption sites

A dilute coverage of Fe atoms ($\approx 50\,\text{atoms}/(100 \times 100\ \text{nm}^2)$) was deposited by evaporation on the $NbSe_2$ sample in the STM at temperatures below 12 K and a base pressure of $1 \cdot 10^{-10}$ mbar. Two distinct apparent heights of the Fe atoms are observed (Fig. S7 and Fig. 1c,d in the main text). Furthermore, the two adatom types differ in the d-level resonances (see blue and orange data in Fig. S8a). Here, only minor differences arise within different atoms of one species.

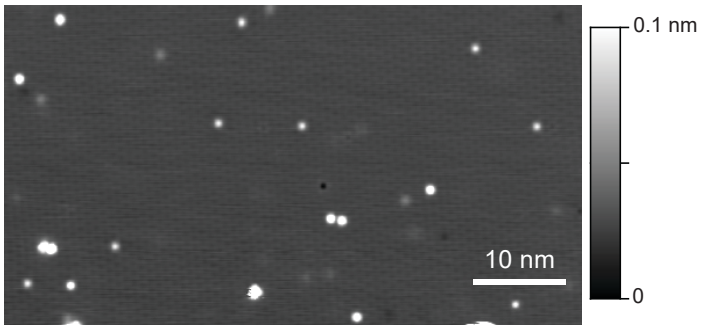

Figure S7: Overview image of the $NbSe_2$ surface after deposition of Fe adatoms (set point: 500 mV, 80 pA).

To identify the precise adsorption site of the two species, we recorded atomic-resolution images as shown in Fig. S8c,d. With the atomic lattice superposed on the STM images we find that all Fe atoms reside in hollow sites of the terminating Se layer. The Fe atoms with large apparent height solely occupy hollow sites, where the neighboring Se atoms form a triangle pointing in one direction, while the atoms with low apparent height are enclosed by a Se triangle rotated by 180°. Inspection of the atomic structure of $NbSe_2$ shows that there are two distinct hollow sites which differ by the presence or absence of a Nb atom beneath (metal-centered, MC, or hollow-centered, HC).

As discussed in the main text, the CDW is incommensurate with the lattice ($a_{\text{cdw}} \simeq 3.05a$[21]) which implies that the CDW smoothly shifts along the atomic lattice of the surface (see Fig. 1a of the main text and Fig. S11). Hence, the maxima of the CDW can be found at different sites with respect to the atomic lattice. Some striking motifs occur when the CDW

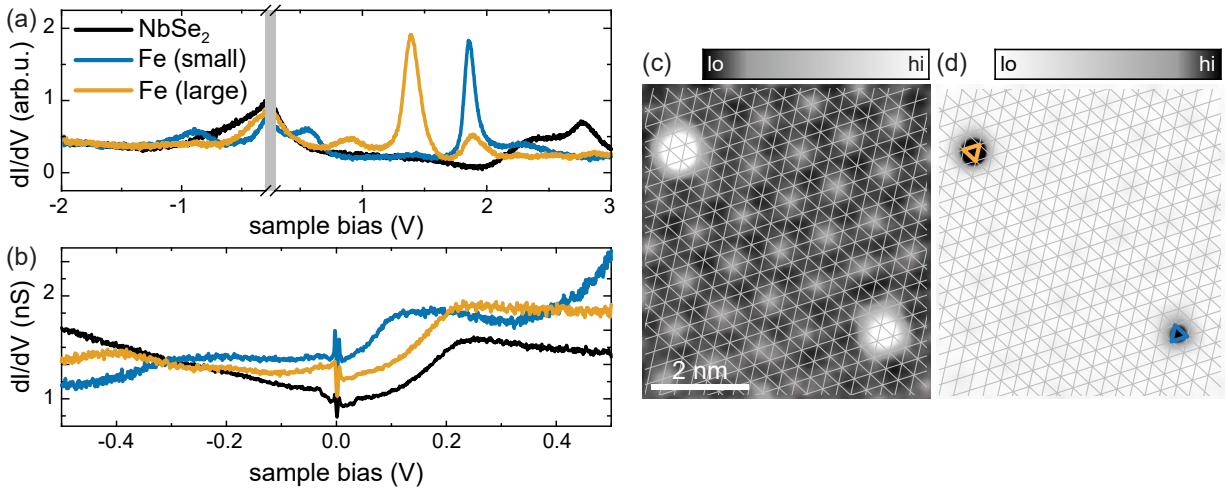

Figure S8: (a) Constant-current ($I = 100$ pA; $V_{\mathrm{rms}} = 5$ mV) spectra of $NbSe_2$ (black) and on Fe adatoms in different hollow sites (blue, orange). (b) Constant-height spectra (set point: $I = 500$ pA, $V = -500$ mV; $V_{\mathrm{rms}} = 2$ mV) of $NbSe_2$ (black) and on Fe adatoms in different hollow sites (blue, orange). (c) Atomic-resolution STM image showing one adatom of each species (set point: 4 mV, 200 pA). The atomic lattice of the top Se layer is overlaid in grey. (d) The same topography and atomic lattice as shown in (c) with an inverted color code such that only the center of the atoms is visible. The orange and blue triangles point out the two different adsorption sites.

maximum coincides with a hollow site (HC) or with a chalcogen site (CC) as illustrated in Fig. 1a of the main manuscript. Interestingly, the configuration with a CDW maximum on a Nb atom (MC) is not observed.[22,23] This local configuration is energetically unfavored.[22–26] To avoid the MC structure smooth grain boundaries are built into the CDW modulation. As illustrated in Fig. S9a,b Fe atoms with small apparent height can be found exactly in the minimum and maximum of the CDW. Hence, this species is assigned to adsorption in the HC position. Consequently, atoms with large apparent height are adsorbed in the MC sites.

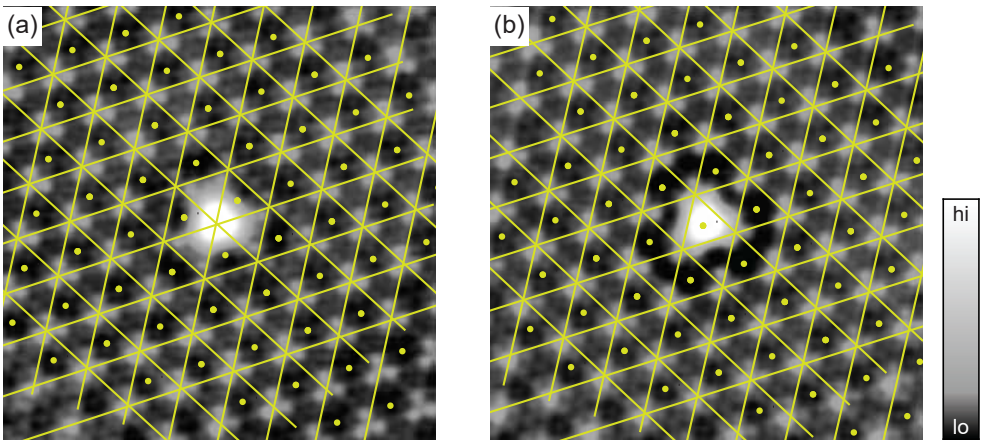

Figure S9: Atomic-resolution STM images of two adatoms with small apparent height, located on the maximum (a) and minimum (b) of the CDW (set point: 4 mV, 200 pA, 8×8 nm^2). The intersections of the yellow grid correspond to maxima, the dots to the minima of the CDW.

Determination of Fe-atom adsorption sites relative to the charge-density wave

The adsorption site of Fe atoms relative to the CDW was determined for a set of approximately 90 atoms (used for the data compilation in Fig. 4a of the main manuscript). The center of the Fe atoms as well as the location of the CDW can be determined from the STM images (see superposed CDW grid on the STM topographies in Fig. S10). The error in placing the CDW grids is estimated as $\delta x = \pm 0.05\, a_{cdw}$, which accounts for the inaccuracy in placing the CDW grid, possible drift effects and for the inaccuracy in finding the center of the atom.

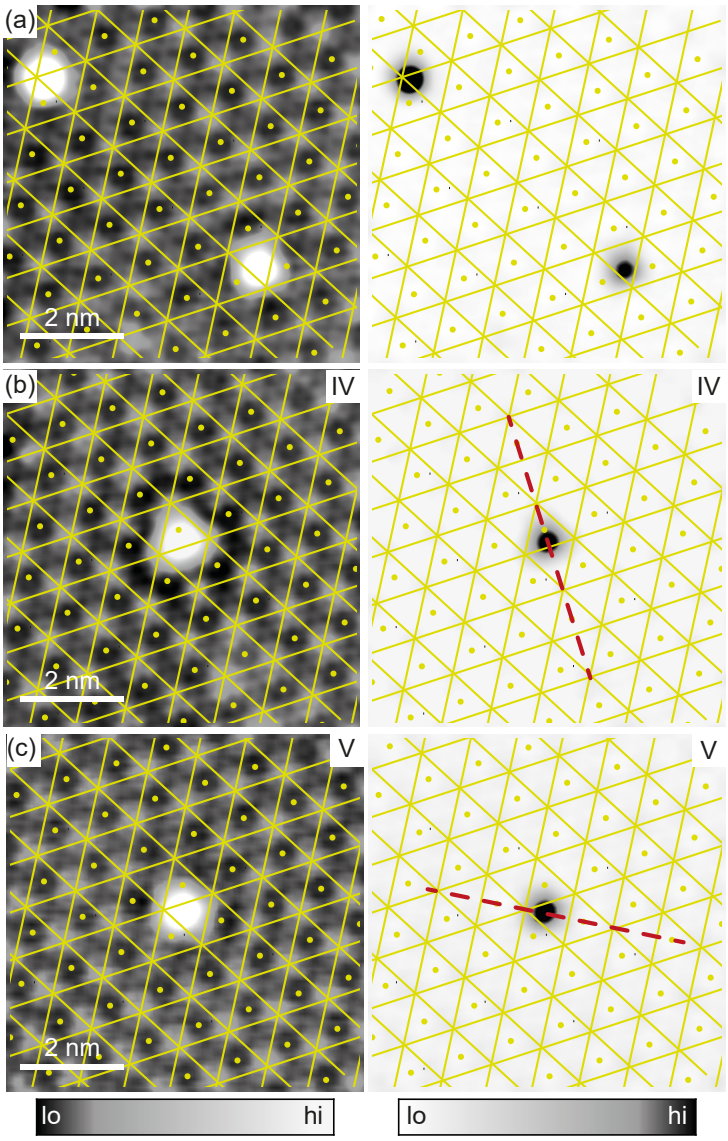

Figure S10: (a-c) The left panels show atomic-resolution topographies overlaid with the CDW lattice (set point: 4 mV, 200 pA). The intersections of the yellow grid correspond to maxima of the CDW, the dots correspond to minima. In the right panel the center of the atoms can be identified (same images as in the left panel with reversed color code). (a) shows both atoms of Fig. 1c. (b) and (c) show atoms IV and V of the main manuscript. Red dashed lines in (b) and (c) indicate the symmetry axis (*cf.* Fig. 3 in the main text).

Pinning of the charge-density wave

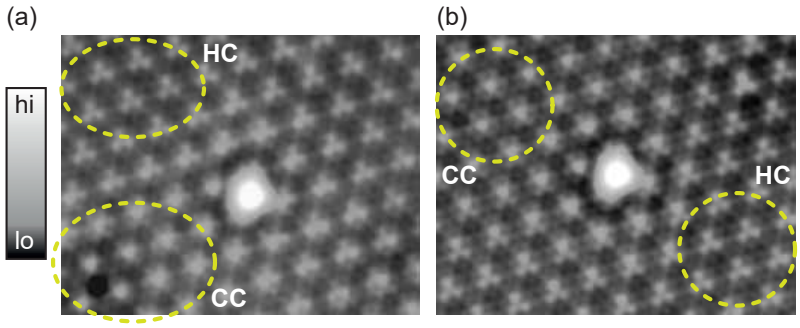

Figure S11: (a,b) Constant-current STM images of two HC adatoms (set point: 4 mV, 200 pA; $9 \times 7\,\mathrm{nm}^2$). A stretched color code is used to resolve the atomic corrugation. Dashed circles indicate pure HC and CC domains. In the bottom left of (a) there is a defect pinning the CC structure.

It has been shown that the CDW can be pinned by crystal defects.[26–30] Therefore, the phase of the CDW is dictated by the complex interplay of lattice defects and long-range order of the CDW. One such example of a local modification of the CDW in the presence of a defect can be seen in Fig. S11a in the bottom left, where the CC structure of the CDW is pinned around a defect (visible as depression). Hence, one may argue that the Fe atoms can affect the CDW. However, a pinning of the CDW by the adatoms is not observed in the experiment. The adatoms seem not to favor a specific CDW domain as can be seen in Fig. S11a and b. Here, pure HC and CC domains are marked. The adatoms are located in the smooth transition region.

Spatial variation of $\mathrm{d}I/\mathrm{d}V$ spectra

Figure S12 shows false-color plots of the $\mathrm{d}I/\mathrm{d}V$ spectra taken along high-symmetry directions of the YSR patterns across atoms I and IV of the main text. The YSR states exhibit long-range intensity oscillations with no detectable variations in energy within our experimental resolution.

We note that in close vicinity to the atom (Figure S13), the intensity variations are particularly strong and some YSR states are accompanied by a negative value of the differential

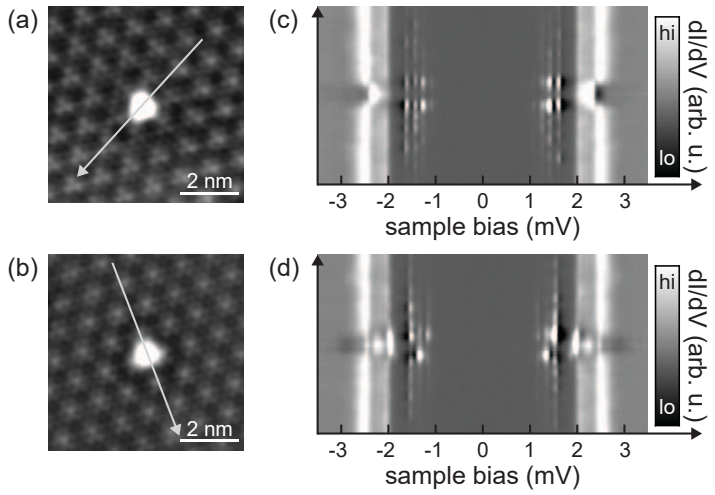

Figure S12: (a,b) Topography of atoms I and IV of the main text (set point: 4 mV, 200 pA). (c,d) Stacked dI/dV spectra (set point: 4 mV, 200 pA; $V_{\mathrm{rms}} = 15$ μeV) taken along the arrows indicated in (a,b).

conductance (NDC) at their high-bias flank. The NDC results from the convolution of YSR states with the tip density of states and can lead to a strong suppression of conductance. In an extreme case, an additional (weak) YSR resonance may be hidden in this part of the spectrum. Examples, where YSR resonances are suppressed below zero are shown by arrows for atom IV, V and VI in Fig. S13. The local variation of the NDC also affects the spatial appearance of the YSR states in the dI/dV maps as is discussed in the following section.

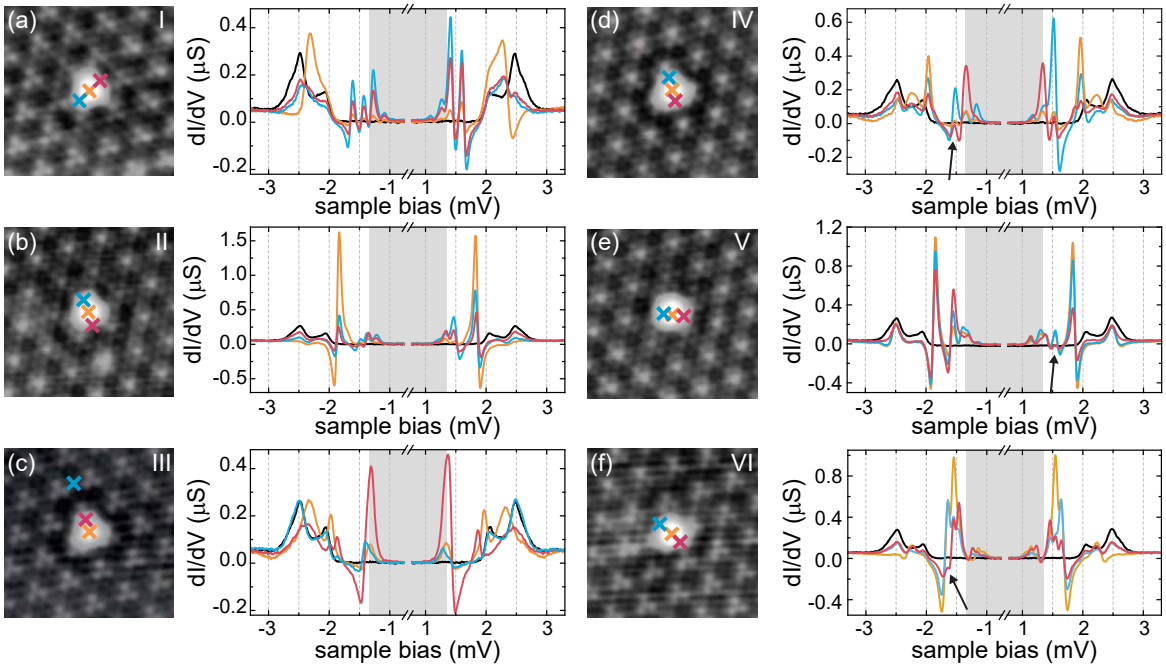

Figure S13: (a-f) Topography (left, $5 \times 5\,\mathrm{nm}^2$) and $\mathrm{d}I/\mathrm{d}V$ spectra (right) taken on and in close vicinity of atoms I-VI of the main text. Colored crosses indicate the location of the spectra (set point: 4 mV, 200 pA; $V_{\mathrm{rms}} = 15\ \mu\mathrm{eV}$). Corresponding substrate data are shown in black for each atom. Black arrows highlight YSR states that are strongly affected by the NDC due to a close-by YSR resonance.

Additional $\mathrm{d}I/\mathrm{d}V$ maps of YSR resonances (both bias polarities and thermal excitations)

Figure S14 shows the complete set of the $\mathrm{d}I/\mathrm{d}V$ maps of atoms I-VI (the positive bias voltage was presented in the main manuscript). $\mathrm{d}I/\mathrm{d}V$ maps at negative bias polarity are depicted in the lower two rows. Opposite bias polarities image the $|u|^2$ and $|v|^2$ components of the YSR states, respectively.[13]

As expected, the $|u|^2$ and $|v|^2$ components lead to distinct scattering patterns. As discussed above, the convolution of tip and sample density of states may lead to distortions of the intensity of individual YSR states, culminating in their suppression in the NDC region of a nearby state. Consequently, also the $\mathrm{d}I/\mathrm{d}V$ maps at the energy of a specific YSR state may be affected by a close-lying YSR state.

In particular, the $\pm\beta$-states of atom II, IV and V are affected by the NDC of the α-resonances, which are close in energy (Fig. S14). One trick to determine and eliminate the effect of NDC is to investigate the $\mathrm{d}I/\mathrm{d}V$ maps of thermally excited YSR states. Thermal excitation of quasiparticles leads to additional resonances within the energy gap of the tip (*cf.* grey shaded area in Fig. 2b,c in the main text). Whereas the original resonances are found at a bias of $eV_{\pm\alpha,\pm\beta} = \pm|\Delta_\mathrm{t} + E_{\alpha,\beta}|$, the thermally excited states are found at $eV_{\pm\alpha^\star,\pm\beta^\star} = \mp|\Delta_\mathrm{t} - E_{\alpha,\beta}|$.[17] The thermally excited YSR states are of much less intensity and, therefore, exhibit a small or negligible region of NDC. Figure S15 shows the $\mathrm{d}I/\mathrm{d}V$ maps recorded at the corresponding voltages of the thermally excited YSR states for atoms I-VI. In these maps the similarity of the $\pm\beta^\star$ states of atoms I, II and IV is more striking than in the original maps of $\pm\beta$. To illustrate the impact of the NDC from the $\pm\alpha$-YSR resonances on the $\pm\beta$ state, we simulate the map of $\pm\beta$ by subtracting a fraction of the $\pm\alpha$ maps (mimicking the NDC) from the $\pm\beta^\star$ maps. The result is compared to the maps at the energies corresponding to $\pm\beta$ (Fig. S16) and shows remarkable similarity, illustrating the impact of NDC.

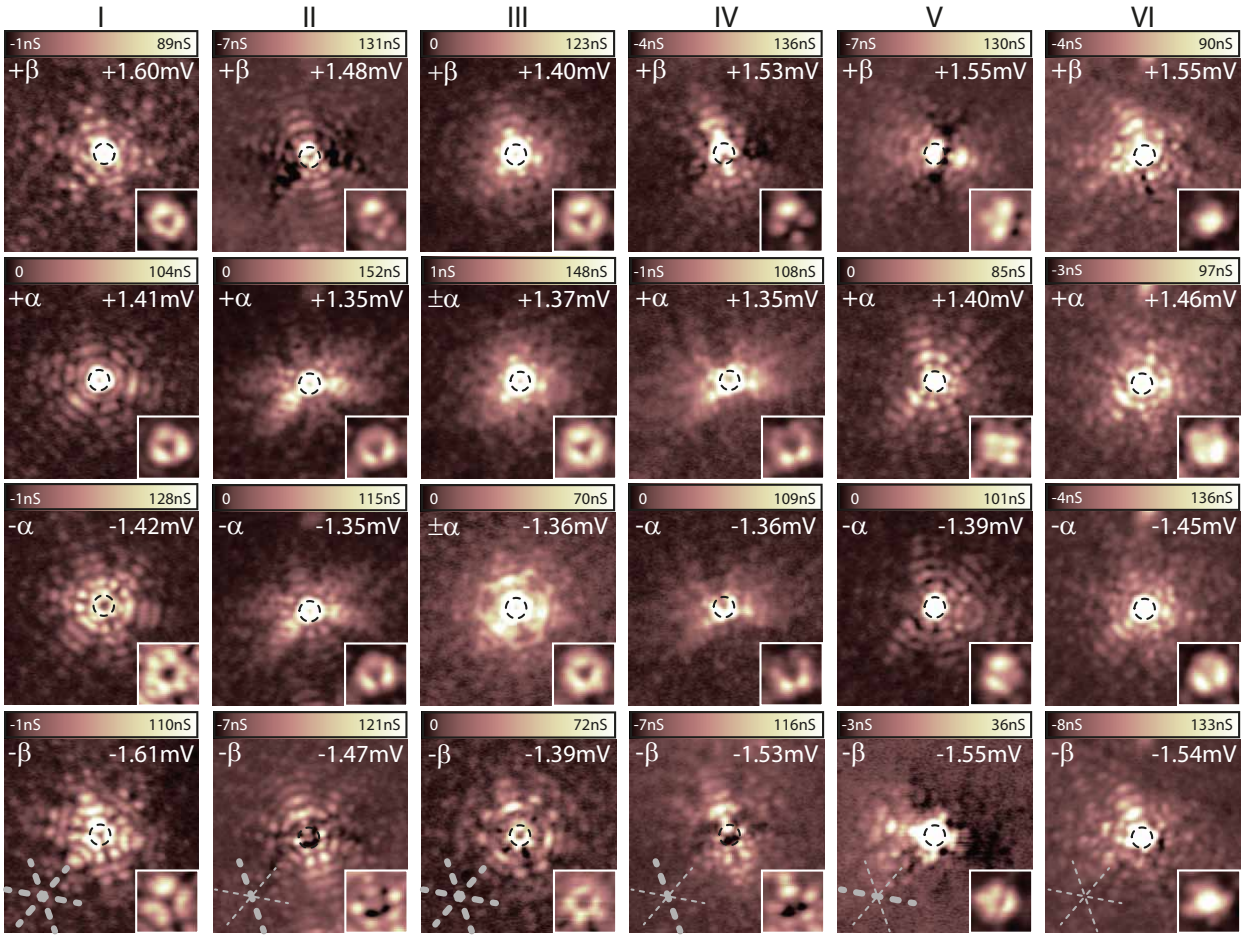

Figure S14: Constant-contour $\mathrm{d}I/\mathrm{d}V$ maps (9.5×9.5 nm^2) of the YSR ($\pm\alpha, \pm\beta$) states of HC atoms I-VI (set point: 4 mV, 200 pA; V_{rms} = 15-25 μeV; V_{bias} as indicated in the images). The insets show a 2×2 nm^2 close-up view around the center of the atoms. Black dashed circles (diameter 1 nm) outline the atoms' position. The grey dashed lines in the bottom map of each atom indicate the crystal's symmetry axes. Thick lines indicate mirror axes present in the $\mathrm{d}I/\mathrm{d}V$ map.

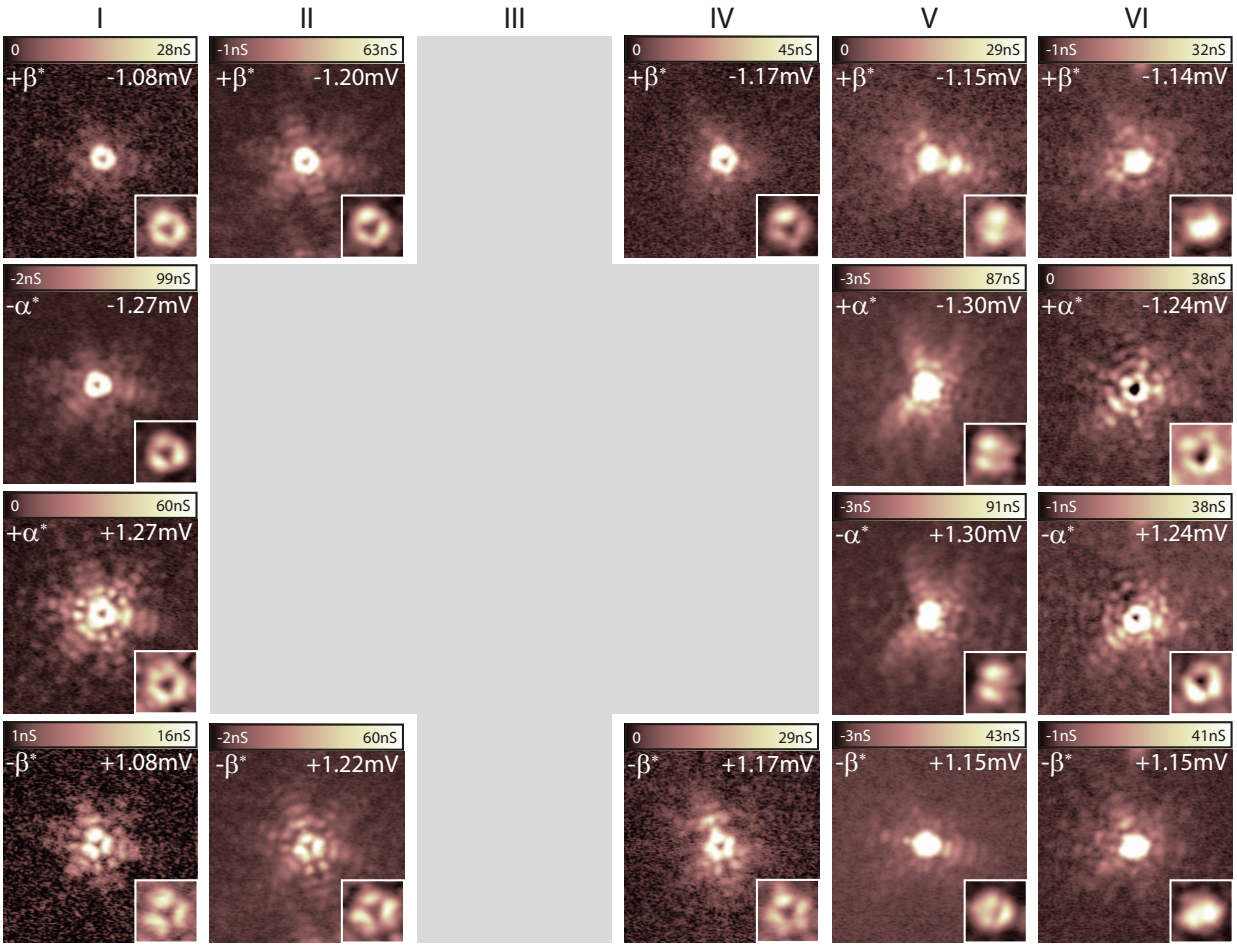

Figure S15: Constant-contour $\mathrm{d}I/\mathrm{d}V$ maps (9.5×9.5 nm^2) of the thermally excited YSR ($\pm\alpha, \pm\beta$) states (set point: 4 mV, 200 pA; V_{rms} = 15-25 μeV; V_{bias} as indicated in the images). The insets show a 2×2 nm^2 close-up view around the center of the atoms. The images are arranged in the same way as in Fig. S14, *i.e.* the maps of the thermally excited YSR states can be found in the same position within the array as in Fig. S14. For YSR resonances at zero energy (*i.e.* $eV_{+\alpha} = eV_{-\alpha} = \Delta_{\mathrm{t}}$) there are no maps of the corresponding thermal excitations (grey area).

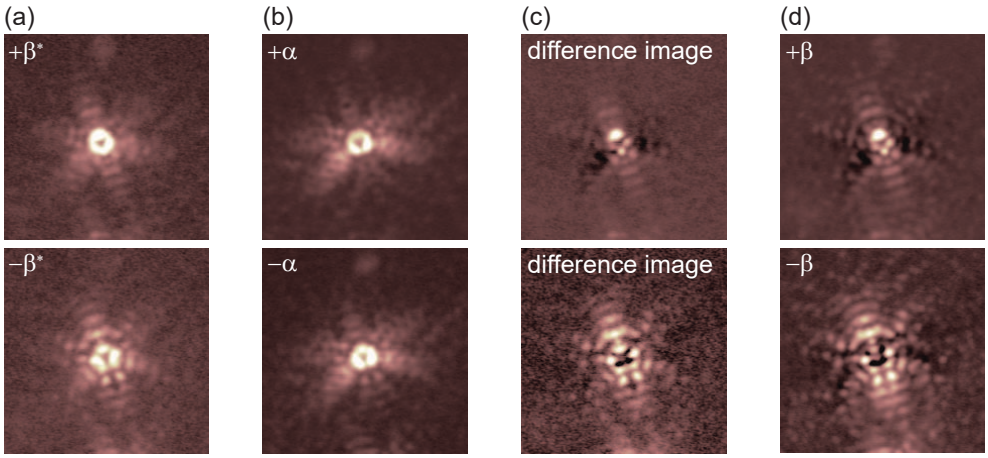

Figure S16: Constant-contour dI/dV maps of (a) $+\beta^\star$ (top) and $-\beta^\star$ (bottom) of atom II (same data can be found in Fig. S15), and (b) $+\alpha$ (top) and $-\alpha$ (bottom) of atom II (same data can be found in Fig. S14). (c) Difference images: $+\alpha$ ($-\alpha$) map subtracted with a factor of 0.7 (1.0) from the map $+\beta^\star$ ($-\beta^\star$). (d) dI/dV map of the $+\beta$ (top) and $-\beta$ (bottom) resonance (same data can be found in Fig. S14). (c) and (d) are very similar.

Determination of YSR energies

To determine the YSR energies, we fit the deconvolved spectra (*cf.* Fig. S6) in the low-energy region with a set of 4 Gaussians (2 pairs of peaks):

$$\begin{aligned}\mathrm{LDOS}(E) = D_0 + A_1 e^{-(E-E_\alpha)^2/(2\sigma^2)} + A_2 e^{-(E+E_\alpha)^2/(2\sigma^2)} \\ + B_1 e^{-(E-E_\beta)^2/(2\sigma^2)} + B_2 e^{-(E+E_\beta)^2/(2\sigma^2)}.\end{aligned} \tag{S22}$$

Here, D_0 is an offset, E_α and E_β are the YSR energies, $A_{1,2}$ and $B_{1,2}$ are four amplitudes and σ is the width of the Gaussian peaks.

The top panel of Fig. S17c shows the extracted energies of the YSR states of approximately 90 atoms with respect to their location relative to the CDW. The error bar in x-direction results from the inaccuracy in finding the exact position relative to the CDW as discussed along with Fig. S10. The error margins of the YSR energy include the uncertainty in the exact value of the tip's energy gap Δ_t, the lock-in modulation of the bias voltage and the standard deviation of the fit routine. Additionally, an error of $\pm\sigma/2$ was added to the energy uncertainty if the peaks are not well separated (*i.e.* $E_\alpha - E_\beta \leq 2\sigma$). This is mainly

the case for atoms close to the CDW minimum, where we cannot distinguish the α- and β-resonances as they are both very close to zero energy (*e.g.* atom III in the main text). Some of these atoms can be fitted with only one pair of Gauss peaks as the YSR states overlap. In this case both energies have the same value ($E_\alpha = E_\beta$).

As discussed in the main manuscript, we find a correlation of the YSR energy with position along the CDW symmetry axis. E_α and E_β are largest at the maximum of the CDW and decrease with distance from the maximum. By default, the fit outputs for E_α and E_β are positive. Assuming that E_α and E_β should follow a similar trend, we suggest that the α-resonance crosses zero energy, *i.e.* undergoes the quantum phase transition.[31] Therefore, $E_\alpha < 0$ was assumed for the atoms in close vicinity to the CDW minimum (*cf.* atom III, the set of atoms with $E_\alpha < 0$ is marked in orange and grey). Having passed the minimum (*cf.* atom IV) the α- and β-states can be separated and identified again in the dI/dV maps (see Fig. 3 in the main manuscript and Figs. S14, S15, S16), *i.e.* $E_\alpha > 0$.

The top panel of Fig. 4a in the main manuscript is obtained from the data in Fig. S17c by averaging over all atoms that are found within an interval of ± 0.05 a_{cdw}. This corresponds to the uncertainty in the determination of the atoms' position with respect to the CDW (see above). The error margins in energy are the standard deviations of the averaging including the average of the errors shown in Fig. S17c.

As seen in Fig. S17 and Fig. 4 of the main text, some regions along the CDW cannot be probed by Fe adatoms (grey areas). To understand the absence of data in these regions, we illustrate the phase change of the CDW (black rhombi) with respect to the atomic lattice (grey lattice) along the main symmetry axis in detail in Fig. S18. A HC adsorption site of an Fe atom is marked by a colored triangle on the atomic lattice. The green triangles indicate observed lattice sites, whereas the red triangles indicate that we did not find these adsorption sites relative to the CDW. The latter cases correspond to configurations, where the maximum of the CDW is located on top of a Nb atom. These so-called MC configurations are energetically disfavored as shown by DFT calculations and do not occur on the surface.[22–26]

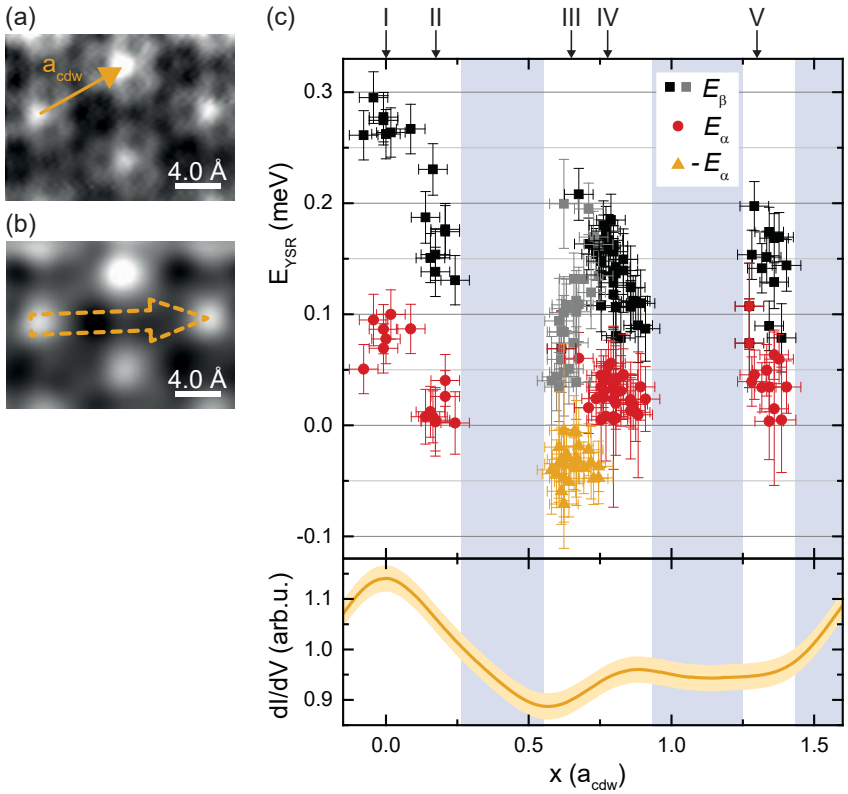

Figure S17: (a) Constant-height $\mathrm{d}I/\mathrm{d}V$ map taken at $T = 8\,\mathrm{K}$ and $V_{\mathrm{bias}} = 0$ (set point: 4 mV, 200 pA; $V_{\mathrm{rms}} = 100$ μeV; some z-drift is visible). (b) FFT-filtered data of (a) (already presented in Fig. 4 in the main text). The signal averaged over the radius of influence of 125 pm, which is approx. the covalent radius of a Fe atom (dashed orange arrow) is plotted in the bottom panel of (c) for one complete period of the CDW. (c) Evaluation of YSR energies E_α, E_β of approximately 90 atoms measured on several samples with several Pb tips by fitting the deconvolved spectra as described in the text. Error bars are also discussed in the text. Black and grey show the evolution of E_β. Red and orange data points correspond to E_α. For the orange data points a negative E_α was assumed. Corridors with no datapoints are marked in gray.

Hence, the corresponding Fe adsorption sites cannot be found either. This explains the absence of data points in the grey areas with only one exception. The third high symmetry position, where an atomic HC adsorption site would sit exactly in the local minimum of the CDW (marked with the red arrow in Fig. S18b), was also not found in experiment. We may speculate that the energy landscape of the CDW can be affected by the Fe adatoms for this specific adsorption site.

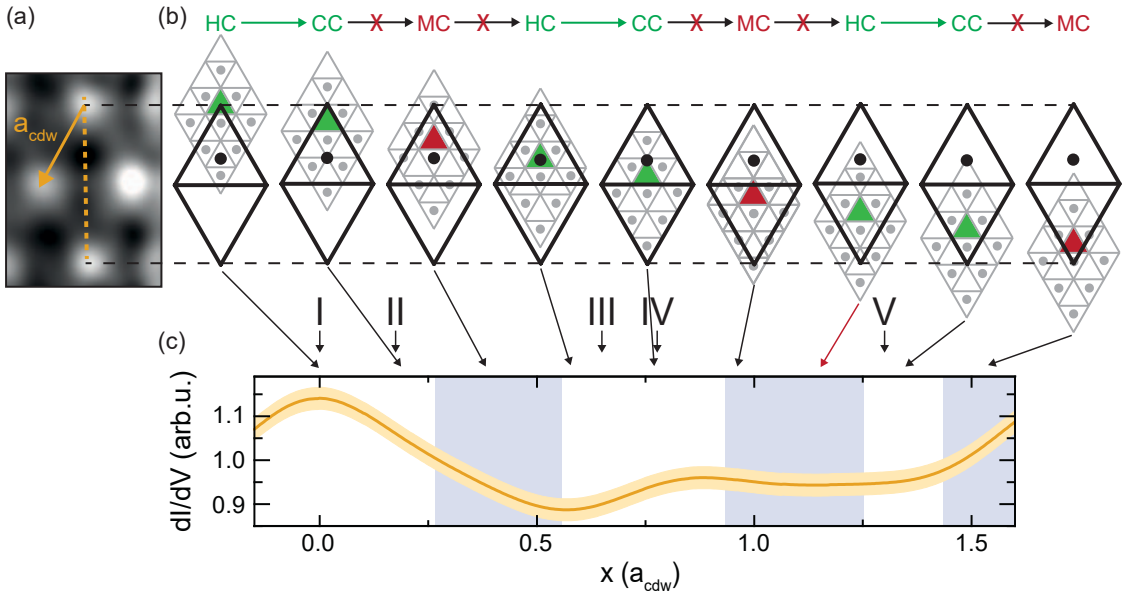

Figure S18: (a) FFT-filtered topography already presented in Fig. S17b and inset of Fig. 4 in the main text. (b) Atomic lattice in grey and CDW lattice in black. Crossing of the atomic lattice represent Se atoms, Nb atoms of the second layer are indicated by the grey dots. Crossings of the CDW lattice correspond to CDW maxima, the black dot indicates the CDW minimum. One HC hollow site is marked in color. Green/red indicates if the relative orientation both lattices relative to each other can be found in experiment. (c) Connection to linecut along the symmetry axis of the CDW (see bottom panel of Fig. S17b and Fig. 4b in the main text).

References

(1) Grüner, G. *Density waves in solids*; CRC Press, 1994.

(2) Smith, N. V.; Kevan, S. D.; DiSalvo, F. J. Band structures of the layer compounds 1T-

TaS_2 and 2H-$TaSe_2$ in the presence of commensurate charge-density waves. *J. Phys. C: Solid State Phys.* **1985**, *18*, 3175–3189.

(3) Rossnagel, K.; Rotenberg, E.; Koh, H.; Smith, N. V.; Kipp, L. Fermi surface, charge-density-wave gap, and kinks in $2H-TaSe_2$. *Phys. Rev. B* **2005**, *72*, 121103.

(4) Inosov, D. S.; Zabolotnyy, V. B.; Evtushinsky, D. V.; Kordyuk, A. A.; Büchner, B.; Follath, R.; Berger, H.; Borisenko, S. V. Fermi surface nesting in several transition metal dichalcogenides. *New J. Phys.* **2008**, *10*, 125027.

(5) Inosov, D. S.; Evtushinsky, D. V.; Zabolotnyy, V. B.; Kordyuk, A. A.; Büchner, B.; Follath, R.; Berger, H.; Borisenko, S. V. Temperature-dependent Fermi surface of $2H$-$TaSe_2$ driven by competing density wave order fluctuations. *Phys. Rev. B* **2009**, *79*, 125112.

(6) Rahn, D. J.; Hellmann, S.; Kalläne, M.; Sohrt, C.; Kim, T. K.; Kipp, L.; Rossnagel, K. Gaps and kinks in the electronic structure of the superconductor $2H$-$NbSe_2$ from angle-resolved photoemission at 1 K. *Phys. Rev. B* **2012**, *85*, 224532.

(7) Ménard, G. C.; Guissart, S.; Brun, C.; Pons, S.; Stolyarov, V. S.; Debontridder, F.; Leclerc, M. V.; Janod, E.; Cario, L.; Roditchev, D.; Simon, P.; Cren, T. Coherent long-range magnetic bound states in a superconductor. *Nature Phys.* **2015**, *11*, 1013.

(8) Bawden, L.; Cooil, S. P.; Mazzola, F.; Riley, J. M.; Collins-McIntyre, L. J.; Sunko, V.; Hunvik, K. W. B.; Leandersson, M.; Polley, C. M.; Balasubramanian, T.; et al., Spin-valley locking in the normal state of a transition-metal dichalcogenide superconductor. *Nature Comm.* **2016**, *7*, 11711.

(9) Xi, X.; Wang, Z.; Zhao, W.; Park, J.-H.; Law, K. T.; Berger, H.; Forró, L.; Shan, J.; Mak, K. F. Ising pairing in superconducting $NbSe_2$ atomic layers. *Nature Phys.* **2016**, *12*, 139–143.

(10) Hewson, A. C. *The Kondo Problem to Heavy Fermions*; Cambridge University Press, 1993.

(11) Yu, L. Bound State in Superconductors With Paramagnetic Impurities. *Acta Phys. Sin.* **1965**, *21*, 75–91.

(12) Shiba, H. Classical Spins in Superconductors. *Prog. Theor. Phys.* **1968**, *40*, 435–451.

(13) Rusinov, A. I. Superconcductivity near a Paramagnetic Impurity. *JETP Lett.* **1969**, *9*, 85.

(14) Moca, C. P.; Demler, E.; Jankó, B.; Zaránd, G. Spin-resolved spectra of Shiba multiplets from Mn impurities in MgB_2. *Phys. Rev. B* **2008**, *77*, 174516.

(15) Kiršanskas, G.; Goldstein, M.; Flensberg, K.; Glazman, L. I.; Paaske, J. Yu-Shiba-Rusinov states in phase-biased superconductor–quantum dot–superconductor junctions. *Phys. Rev. B* **2015**, *92*, 235422.

(16) Shiba, H. Classical Spins in Superconductors. *Prog. Theor. Phys.* **1968**, *40*, 435–451.

(17) Ruby, M.; Pientka, F.; Peng, Y.; von Oppen, F.; Heinrich, B. W.; Franke, K. J. Tunneling Processes into Localized Subgap States in Superconductors. *Phys. Rev. Lett.* **2015**, *115*, 087001.

(18) Tersoff, J.; Hamann, D. R. Theory of the scanning tunneling microscope. *Phys. Rev. B* **1985**, *31*, 805–813.

(19) Ruby, M.; Heinrich, B. W.; Pascual, J. I.; Franke, K. J. Experimental Demonstration of a Two-Band Superconducting State for Lead Using Scanning Tunneling Spectroscopy. *Phys. Rev. Lett.* **2015**, *114*, 157001.

(20) Choi, D.-J.; Rubio-Verdú, C.; De Bruijckere, J.; Ugeda, M. M.; Lorente, N.; Pascual, J. I. Mapping the orbital structure of impurity bound states in a superconductor. *Nature Commun.* **2017**, *8*, 15175.

(21) Soumyanarayanan, A.; Yee, M. M.; He, Y.; van Wezel, J.; Rahn, D. J.; Rossnagel, K.; Hudson, E. W.; Norman, M. R.; Hoffman, J. E. Quantum phase transition from triangular to stripe charge order in $NbSe_2$. *Proc. Natl. Acad. Sci.* **2013**, *110*, 1623–7.

(22) Gye, G.; Oh, E.; Yeom, H. W. Topological Landscape of Competing Charge Density Waves in $2H-NbSe_2$. *Phys. Rev. Lett.* **2019**, *122*, 016403.

(23) Guster, B.; Rubio-Verdú, C.; Robles, R.; Zaldívar, J.; Dreher, P.; Pruneda, M.; Silva-Guillén, J. Á.; Choi, D.-J.; Pascual, J. I.; Ugeda, M. M.; Ordejón, P.; Canadell, E. Coexistence of Elastic Modulations in the Charge Density Wave State of $2H$-$NbSe_2$. *Nano Lett.* **2019**, *19*, 3027–3032.

(24) Zheng, F.; Zhou, Z.; Liu, X.; Feng, J. First-principles study of charge and magnetic ordering in monolayer $NbSe_2$. *Phys. Rev. B* **2018**, *97*, 081101.

(25) Lian, C. S.; Si, C.; Duan, W. Unveiling Charge-Density Wave, Superconductivity, and Their Competitive Nature in Two-Dimensional $NbSe_2$. *Nano Letters* **2018**, *18*, 2924–2929.

(26) Cossu, F.; Moghaddam, A. G.; Kim, K.; Tahini, H. A.; Di Marco, I.; Yeom, H.-W.; Akbari, A. Unveiling hidden charge density waves in single-layer $NbSe_2$ by impurities. *Phys. Rev. B* **2018**, *98*, 195419.

(27) Langer, M.; Kisiel, M.; Pawlak, R.; Pellegrini, F.; Santoro, G. E.; Buzio, R.; Gerbi, A.; Balakrishnan, G.; Baratoff, A.; Tosatti, E.; Meyer, E. Giant frictional dissipation peaks and charge-density-wave slips at the $NbSe_2$ surface. *Nat. Mater.* **2014**, *13*, 173–177.

(28) Flicker, F.; van Wezel, J. Charge order from orbital-dependent coupling evidenced by $NbSe_2$. *Nature Commun.* **2015**, *6*, 7034.

(29) Chatterjee, U.; Zhao, J.; Iavarone, M.; Di Capua, R.; Castellan, J. P.; Karapetrov, G.;

Malliakas, C. D.; Kanatzidis, M. G.; Claus, H.; Ruff, J. P. C.; et al., Emergence of coherence in the charge-density wave state of 2H-$NbSe_2$. *Nat. Commun.* **2015**, *6*, 6313.

(30) Arguello, C. J.; Chockalingam, S. P.; Rosenthal, E. P.; Zhao, L.; Gutiérrez, C.; Kang, J. H.; Chung, W. C.; Fernandes, R. M.; Jia, S.; Millis, A. J.; Cava, R. J.; Pasupathy, A. N. Visualizing the charge density wave transition in $2H$-$NbSe_2$ in real space. *Phys. Rev. B* **2014**, *89*, 235115.

(31) Franke, K. J.; Schulze, G.; Pascual, J. I. Competition of Superconducting Phenomena and Kondo Screening at the Nanoscale. *Science* **2011**, *332*, 940–944.